Evaluation of DEM-assisted SAR coregistration

D. O. Nitti[a,b], R. F. Hanssen[b], A. Refice[c], F. Bovenga[c], G. Milillo[d] and R. Nutricato[a]

[a]Dipartimento Interateneo di Fisica, Politecnico di Bari, Via Amendola 173, 70126 Bari, Italy
[b]DEOS - Delft University of Technology - Kluyverweg 1, 2629 HS Delft, The Netherlands
[c]ISSIA-CNR, Via Amendola 122/d, 70126 Bari, Italy
[d]ASI-CGS, Loc. Contrada Terlecchia P.O.Box A.D.P, 75100 Matera, Italy

ABSTRACT

Image alignment is without doubt the most crucial step in SAR Interferometry. Interferogram formation requires images to be coregistered with an accuracy of better than 1/8 pixel to avoid significant loss of phase coherence. Conventional interferometric precise coregistration methods for full-resolution SAR data (Single-Look Complex imagery, or SLC) are based on the cross-correlation of the SLC data, either in the original complex form or as squared amplitudes. Offset vectors in slant range and azimuth directions are computed on a large number of windows, according to the estimated correlation peaks. Then, a two-dimensional polynomial of a certain degree is usually chosen as warp function and the polynomial parameters are estimated through LMS fit from the shifts measured on the image windows. In case of rough topography and long baselines, the polynomial approximation for the warp function becomes inaccurate, leading to local misregistrations. Moreover, these effects increase with the spatial resolution and then with the sampling frequency of the sensor, as first results on TerraSAR-X interferometry confirm. An improved, DEM-assisted image coregistration procedure can be adopted for providing higher-order prediction of the offset vectors. Instead of estimating the shifts on a limited number of patches and using a polynomial approximation for the transformation, this approach computes pixel by pixel the correspondence between master and slave by using the orbital data and a reference DEM. This study assesses the performance of this approach with respect to the standard procedure. In particular, both analytical relationships and simulations will evaluate the impact of the finite vertical accuracy of the DEM on the final coregistration precision for different radar postings and relative positions of satellites. The two approaches are compared by processing real data at different carrier frequencies and using the interferometric coherence as quality figure.

Keywords: Synthetic Aperture Radar (SAR), interferometry, coregistration, Digital Elevation Model (DEM).

1. INTRODUCTION

Synthetic Aperture Radar Interferometry (InSAR) is the study of coherent combinations of SAR images taken from slightly different observation directions. Precise (sub-pixel)[1] co-registration is then required as first processing step. This is a non-trivial task, since a change in radar acquisition geometry generates image shifts which depend on the topography.[2] One of the most used approaches relies on the fact that SAR images suitable for interferometry are separated by relatively small geometric baselines (compared e.g. to radargrammetric processing[2]). In this case, when topographic variations are not too strong, the change in acquisition geometry from one image to the other can be approximated by a low-order polynomial transformation.

For rough topography, however, this polynomial model is hardly sufficient, and a more complex model depending on the topography, should be used to ensure the required coregistration precision. Moreover, misregistrations due to the smoothness of the polynomial warp model are more significant when increasing the normal baseline, thus becoming unacceptable, especially for the new X-band SAR satellites (TerraSAR, COSMO/SkyMed), because of their higher spatial resolutions and sampling rates with respect to ESA C-band sensors (ERS, ENVISAT). Various groups reported experiences with DEM-based coregistration approaches applied to conventional InSAR techniques,[3,4] detecting some improvement w.r.t. more conventional methods, although to date such assessments have been rather empirical.

Send correspondence to D.O. Nitti, E-mail: davide.nitti@fisica.uniba.it, Telephone: +39 080 5442396

Image and Signal Processing for Remote Sensing XIV, edited by
Lorenzo Bruzzone, Claudia Notarnicola, Francesco Posa, Proc. of SPIE Vol. 7109
710919 · © 2008 SPIE · CCC code: 0277-786X/08/$18 · doi: 10.1117/12.802767

This study intends to assess the performance of this approach with respect to the conventional procedure based on cross-correlations and the approximated polynomial warp function. We refer to a DEM-assisted technique developed at TU Delft[3] and included in the DORIS open-source SAR interferometric processing tool.[5]

The paper is organized as follows. In Sec. 2 the geometrical model is described and the analytical formulation of the relative shifts between two images are computed as a function of the known mission parameters. Section 3 provides the results obtained by simulating different acquisition configurations. In particular the effect of the DEM errors on the final coregistration precision is evaluated. In Sec. 4 the conventional coregistration procedure and the DEM-assisted coregistration procedure are compared by processing real data acquired at L, C, and X band. Comments and conclusions are provided in Sec. 5.

2. ANALYTICAL FORMULATION

The following formulation illustrates the analytical estimation of the slant range offset between two SAR images, assuming exact knowledge of the position of the satellite during the two acquisitions as well as the topographic profile of the imaged scene. Let us start with a description of the geometrical model adopted.

2.1 Geometrical approach

Because of the flattening of the Earth, an ellipsoid (such as WGS84) is much more accurate than a sphere for modeling the Earth geometrically. Nevertheless, as we will show, spherical models can be used as a good approximation of the local ellipsoidal surface, limited to the swath extension, with negligible errors.

In this section we introduce a spherical model (Fig. 1a) that will be further refined in Sec. 2.2. All geometric parameters involved in the following discussion have to be computed in an ECEF (*Earth Centered Earth Fixed*) reference system $Oxyz$ (see Fig. 2a), thus intrinsically taking into account the effect of the Earth's rotation. First of all, instead of assuming a constant mean value for the Earth's radius ρ during the satellite's orbit around the Earth, we will choose a value "tuned" to the master image slow time (or azimuth time), since Earth curvature for a generic point on the ground w.r.t. any cross section is a function of the geodetic latitude (not of the longitude, because of the symmetry of the ellipsoid). Therefore, once the master slow time instant is fixed, a good choice for the radius ρ of the spherical model can be the Earth curvature radius R_{az} of the nadir projection of the master satellite position on the reference ellipsoid (P_M^{nad}, with geodetic coordinates Φ_M and Λ_M) w.r.t. the zero-Doppler plane π, because of the side-looking acquisition mode of SAR sensors and the assumption of zero-Doppler (deskewed) stripmap imaging geometry (Fig. 2). The azimuth angle of the cross section π is therefore equal to $(\alpha_h + \pi/2)$ (in case of right looking), where α_h is the inclination, or heading, of the orbit (measured clockwise from the north direction). The Earth curvature R_{az} corresponding to the section π is equal to (Euler's theorem):[6]

$$\frac{1}{R_{\mathrm{az}}} = \frac{\cos^2(\alpha_h + \frac{\pi}{2})}{M} + \frac{\sin^2(\alpha_h + \frac{\pi}{2})}{N}, \tag{1}$$

where M and N are the radii of curvature of the meridian and the prime vertical, respectively, for the specific point $P_M^{\mathrm{nad}}(\Phi_M,\Lambda_M)$ considered:

$$M = \frac{a(1-e^2)}{\sqrt[3]{1-e^2\sin^2\Phi_M}}, \qquad N = \frac{a}{\sqrt{1-e^2\sin^2\Phi_M}} \quad \text{(Meusnier's theorem[7])}. \tag{2}$$

and a, b and e are the semi-axes and the first eccentricity of the reference ellipsoid.

In other words, for each master slow time instant, the cross section between the corresponding zero-Doppler plane π and the reference ellipsoid is an ellipse that we are approximating, nearby the projection P_M^{nad}, by a circle of radius $\rho = R_{\mathrm{az}}$, centered on the curvature center $\tilde{O}$ of the ellipse w.r.t. P_M^{nad}, by assuming that such an approximation is still acceptable for all points on the ellipse belonging to the image swath. Therefore, for every point along the ground swath, the difference between the heights above the spherical approximation, H_G,

and the reference ellipsoid, h_G, is assumed negligible (Fig. 1). In the zero-Doppler plane π, we define a reference system $\tilde{O}\tilde{x}\tilde{y}\tilde{z}$ (see Fig. 2), with origin in $\tilde{O}$, whose coordinates in the $Oxyz$ reference system are:

$$\begin{bmatrix} x_{\tilde{O}} \\ y_{\tilde{O}} \\ z_{\tilde{O}} \end{bmatrix} = \begin{bmatrix} r_{x\tilde{x}} & r_{x\tilde{y}} & r_{x\tilde{z}} \\ r_{y\tilde{x}} & r_{y\tilde{y}} & r_{y\tilde{z}} \\ r_{z\tilde{x}} & r_{z\tilde{y}} & r_{z\tilde{z}} \end{bmatrix} \begin{bmatrix} 0 \\ 0 \\ N - R_{az} \end{bmatrix} + \begin{bmatrix} 0 \\ 0 \\ \frac{-\tan\Phi_M(a^2-b^2)}{\sqrt{a^2+b^2\tan^2\Phi_M}} \end{bmatrix}, \tag{3}$$

where the matrix of coefficients $r_{i\tilde{j}}$ is given by:

$$\begin{bmatrix} r_{x\tilde{x}} & r_{x\tilde{y}} & r_{x\tilde{z}} \\ r_{y\tilde{x}} & r_{y\tilde{y}} & r_{y\tilde{z}} \\ r_{z\tilde{x}} & r_{z\tilde{y}} & r_{z\tilde{z}} \end{bmatrix} = \begin{bmatrix} \sin\Lambda_M & \cos\Lambda_M & 0 \\ -\cos\Lambda_M & \sin\Lambda_M & 0 \\ 0 & 0 & 1 \end{bmatrix} \begin{bmatrix} 1 & 0 & 0 \\ 0 & \sin\Phi_M & \cos\Phi_M \\ 0 & -\cos\Phi_M & \sin\Phi_M \end{bmatrix} \begin{bmatrix} -\cos\alpha_h & -\sin\alpha_h & 0 \\ \sin\alpha_h & -\cos\alpha_h & 0 \\ 0 & 0 & 1 \end{bmatrix}. \tag{4}$$

The $\tilde{z}$ axis is coincident with the zenithal direction of the master satellite position, while the $\tilde{x}$ axis is normal to the first one, directed towards the looking direction of the radar.

In theory, precise orbits and a Digital Elevation Model, radarcoded in master geometry, are sufficient for retrieving analytically the offset between master and slave along the slant range direction at each specific master slow time instant, as described further on, where a negligible convergence between master and slave orbits and zero-Doppler geometry has been assumed for simplicity.

The aim is to estimate, for each master pixel number p_M, the corresponding slave pixel position number p_S and so the relative offset in range $\Delta p = p_S - p_M$. Actually, we are interested in evaluating the influence of the baseline (in particular its normal component) on the range offsets. Therefore, a description of the slave satellite position in terms of relative position w.r.t. the master satellite is preferable. With B we indicate the distance (baseline) between master and slave, while α is the off-nadir baseline orientation angle, measured towards the SAR looking direction. Slave height H_S is related to master height H_M, baseline and baseline orientation angle by the following relation:

$$\rho + H_S = \sqrt{(\rho + H_M)^2 + B^2 - 2B(\rho + H_M)\cos\alpha}. \tag{5}$$

For a given pixel number p_σ (where $p_\sigma = 0 \ldots (N_{p_\sigma} - 1)$ and $\sigma \in \{M, S\}$, with $M =$ *"Master"*, $S =$ *"Slave"*), master and slave slant range distances $R_{\sigma,G}$ are related to the corresponding 2-way zero-Doppler range times τ_{p_σ} (or fast times) through:

$$\tau_{p_\sigma} = \tau_{\sigma 0} + \frac{p_\sigma}{f_s}, \qquad R_{\sigma,G} = \frac{c}{2}\tau_{p_\sigma} = \frac{c}{2}(\tau_{\sigma 0} + \frac{p_\sigma}{f_s}), \qquad (\sigma \in \{M, S\}), \tag{6}$$

where c is the speed of light, f_s the range sampling rate and $\tau_{\sigma 0}$ ($\sigma \in \{M, S\}$) are the 2-way zero-Doppler range times for the first range pixels. Pixel offsets between master and slave along range direction are hence given by:

$$\begin{aligned} \Delta p = p_S - p_M = \\ = f_s(2\frac{R_{S,G}}{c} - \tau_{S0}) - p_M = \\ = f_s\big(\frac{2}{c}(R_{S,G} - R_{M,G}) + (\tau_{M0} - \tau_{S0})\big). \end{aligned} \tag{7}$$

Then, for a given master–slave configuration, the offset between master and slave is directly proportional to the range sampling rate. For each master pixel p_M, the main problem is finally the estimation of the distance $R_{S,G}$ between the slave satellite and the ground point G, whose height above the spherical model and distance from the master satellite are equal to H_G and $R_{M,G}$, respectively. This can be accomplished by observing that (Fig. 1a):

$$\begin{gathered} \frac{\sin\delta_{M,S}}{B} = \frac{\sin\alpha}{\rho + H_S}, \qquad \frac{\sin\delta_{M,G}}{R_{M,G}} = \frac{\sin\theta_{M,G}}{\rho + H_G}, \qquad \frac{\sin(\delta_{M,G} - \delta_{M,S})}{R_{S,G}} = \frac{\sin\theta_{S,G}}{\rho + H_G}, \\ \cos^2\theta_{\sigma,G} = \frac{(\rho + H_\sigma)^2 + R_{\sigma,G}^2 - (\rho + H_G)^2}{2R_{\sigma,G}(\rho + H_\sigma)} \qquad (\sigma \in \{M, S\}), \end{gathered} \tag{8}$$

where $\delta_{\sigma,G}$ and $\theta_{\sigma,G}$ (with $\sigma \in \{M, S\}$) are the look angles of the ground point G from, respectively, the curvature center $\tilde{O}$ and the satellites positions (Fig. 1a). For each master pixel p_M, $R_{M,G}$ is expressed by eq. (6) and $R_{S,G}$ can be estimated numerically by combining eq. (8) into:

$$\begin{aligned} &\arcsin \frac{R_{M,G}}{\rho + H_G} \sqrt{1 - \frac{(\rho + H_M)^2 + R_{M,G}^2 - (\rho + H_G)^2}{2R_{M,G}(\rho + H_M)}} \\ &- \arcsin \frac{R_{S,G}}{\rho + H_G} \sqrt{1 - \frac{(\rho + H_S)^2 + R_{S,G}^2 - (\rho + H_G)^2}{2R_{S,G}(\rho + H_S)}} = \arcsin \frac{B \sin \alpha}{\rho + H_S}, \end{aligned} \tag{9}$$

to solve for $R_{S,G}$. In the above expressions, the baseline B and baseline orientation angle α have been used, instead of the parallel and normal components of the baseline, since the latter are functions of the look angle $\theta_{M,G}$. Their expressions are:

$$\begin{aligned} B_\perp &= B \sin(\alpha - \theta_{M,G}), \quad & B \sin \alpha &= B_\perp \cos \theta_{M,G} + B_\parallel \sin \theta_{M,G}, \\ B_\parallel &= B \cos(\alpha - \theta_{M,G}), \quad & B \cos \alpha &= B_\parallel \cos \theta_{M,G} - B_\perp \sin \theta_{M,G}. \end{aligned} \tag{10}$$

In case $|B_\parallel| \ll |B_\perp| \approx B$ or $|B_\perp| \ll |B_\parallel| \approx B$, eq. (9) can be simplified in the following way, as expected:

$$R_{S,G} \approx \begin{cases} R_{M,G} - B_\parallel & \text{if } |B_\parallel| \gg |B_\perp|, \\ \sqrt{R_{M,G}^2 + B_\perp^2} & \text{if } |B_\parallel| \ll |B_\perp|. \end{cases} \tag{11}$$

In brief, the offset between master and slave can be expressed, through eqs. (7)–(9), as the product of the range sampling rate and a function of the normal and parallel baselines, as well as the topographic height H_G above the spherical model adopted (by assumption, very close to the height h_G above the reference ellipsoid).

2.2 Geometrical Model Refinement

The spherical model introduced in the previous section assumes implicitly that the curvature center of the elliptic cross section π (Fig. 2a) corresponding to a point generically selected along the swath extension is coincident or, at least, very close to the origin $\tilde{O}$, that is the curvature center w.r.t. the nadir projection of the master satellite position P_M^{nad}. This approximation is acceptable only for very low geodetic latitudes (e.g. Tanzania – see Sec. 4.1) since, near the Equator, the orbital heading α_h is not too far from $(0, 180)$ degrees (depending on the orbital pass direction, whether ascending or descending) and, therefore, the zero-Doppler plane π is roughly parallel to the prime vertical section. Since, for any point located near to the Equator, its prime vertical section is, in turn, roughly parallel to the equatorial plane, the eccentricity of the corresponding elliptic cross section is very close to 1. For high latitudes, however, a model refinement is necessary. In this case, indeed, by evaluating the distance between a generic ground point and the origin $\tilde{O}$, its variation along a swath extension of 100 km (ERS) may reach also hundreds of meters. Actually, the spherical approximation so far introduced can be still adopted, provided the height above the reference ellipsoid of any ground point G along the swath (h_G), is preliminary converted into the corresponding value above the spherical model (H_G). In order to avoid such a conversion, the optimal spherical approximation should ensure a negligible difference ($H_G - h_G$), for any ground point G. Because of the side-looking acquisition geometry, this can be obtained with a circle whose center C_{mr} and radius $\tilde{\rho}$ are equal, respectively, to the center and radius of curvature of the elliptic cross section corresponding to the point $P_{\text{mr}}^{\text{nad}}$ located at the swath middle range, instead of the master nadir projection P_M^{nad} (see Fig. 2b). Simulations show that this approximation is valid at any latitude, since the distance between a generic point on the ellipse from near to far range on the swath extension and the curvature center C_{mr} differs from the radius $\tilde{\rho}$ by no more than half centimeter for the case of a 100 km swath extension, which is the widest one among the sensors considered here. The model is also valid for wider swaths, such as in the case of the future Sentinel-1 mission ($\sim$ 250 km) for the Interferometric Wide Swath Mode.

The position of the center C_{mr} can be easily derived once an analytical expression for the elliptic cross section in the zero-Doppler plane π has been retrieved. With respect to the $\tilde{O}\tilde{x}\tilde{z}$ reference system, the elliptic cross

section (whose semi-axes $\hat{a}$ and $\hat{b}$ and first eccentricity $\hat{e}$ are different in general from those of the reference ellipsoid) is described by the following equation:

$$\frac{(r_{x\tilde{x}}\tilde{x} + r_{x\tilde{z}}\tilde{z} + x_{\tilde{O}})^2}{a^2} + \frac{(r_{y\tilde{x}}\tilde{x} + r_{y\tilde{z}}\tilde{z} + y_{\tilde{O}})^2}{a^2} + \frac{(r_{z\tilde{x}}\tilde{x} + r_{z\tilde{z}}\tilde{z} + z_{\tilde{O}})^2}{b^2} = 1, \tag{12}$$

where the coefficients $r_{i\tilde{j}}$ are given by (4).

Once a rotation and translation of the $\tilde{O}\tilde{x}\tilde{z}$ axes are performed in order to make them coincident with the ellipse axes (coordinate system $\hat{O}\hat{x}\hat{z}$ in Fig. 2b), the coordinates of the curvature center $C_{\rm mr}$ are given by:

$$\hat{x}_{C_{\rm mr}} = \hat{x}_{P_{\rm mr}^{\rm nad}} - \frac{\hat{a}(1-\hat{e}^2)\cos\varphi_{P_{\rm mr}^{\rm nad}}}{\sqrt[3]{1-\hat{e}^2\sin^2\varphi_{P_{\rm mr}^{\rm nad}}}}, \qquad \hat{y}_{C_{\rm mr}} = \hat{y}_{P_{\rm mr}^{\rm nad}} - \frac{\hat{a}(1-\hat{e}^2)\sin\varphi_{P_{\rm mr}^{\rm nad}}}{\sqrt[3]{1-\hat{e}^2\sin^2\varphi_{P_{\rm mr}^{\rm nad}}}}, \tag{13}$$

where $P_{\rm mr}^{\rm nad}$ is the projection on the ellipse of the ground point at middle range, G_{mr}, and the angle $\varphi_{P_{\rm mr}^{\rm nad}}$ (Fig. 2b) should not be confused with the geodetic latitude of $P_{\rm mr}^{\rm nad}$, since the zero-Doppler plane π is not coincident in general with the prime meridian section.

As mentioned, our aim is to estimate, for each master pixel p_M, the corresponding range offset between master and slave or, equivalently, see eq. (7), the distance $R_{S,G}$ between the slave satellite and the ground point G. Assuming the position of $C_{\rm mr}$ in the $\tilde{O}\tilde{x}\tilde{z}$ reference system has been retrieved for a generic master slow time, the distance $R_{S,G}$ can be estimated more accurately in the refined geometrical model just described. Actually, eq. (9) is still valid, provided the following substitutions are made:

$$\alpha \rightarrow (\alpha - \beta), \qquad (\rho + H_M) \rightarrow R_{C,M}, \qquad (\rho + H_S) \rightarrow R_{C,S}, \qquad (\rho + H_G) \rightarrow (\tilde{\rho} + H_G), \tag{14}$$

where the height H_G above the spherical model for a generic point G along the swath extension may be further replaced with the corresponding value h_G above the reference ellipsoid, thanks to the refined spherical model described in this section, and

$$R_{C,M} = \sqrt{R_{\tilde{O},M}^2 + R_{\tilde{O},C}^2 - 2R_{\tilde{O},M}\,R_{\tilde{O},C}\cos\delta_{M,C}}\,, \qquad R_{C,S} = \sqrt{R_{\tilde{O},S}^2 + R_{\tilde{O},C}^2 - 2R_{\tilde{O},S}\,R_{\tilde{O},C}\cos(\delta_{M,C} - \delta_{M,S})}\,,$$

$$R_{\tilde{O},S} = \sqrt{R_{\tilde{O},M}^2 + B^2 - 2BR_{\tilde{O},M}\cos\alpha}\,, \qquad \sin\beta = \frac{R_{\tilde{O},C}}{R_{C,M}}\sin\delta_{M,C}\,, \qquad \sin\delta_{M,S} = \frac{B}{R_{\tilde{O},S}}\sin\alpha\,,$$

are all known quantities and not dependent on the master pixel considered.

3. SIMULATIONS RESULTS

Traditional SAR image registration methods are based on the estimation of azimuth and range warp functions, mapping the slave onto the master image in both directions. In general, such functions are modeled as 2-D polynomials of a certain degree. Because of their smoothness, they well approximate the true geometric distortions only at low normal baselines and for gentle topography, especially for sensors with higher range sampling rate, as will be shown in the next section. The sensitivity of the DEM-assisted coregistration to the DEM vertical accuracy will be discussed in Sec. 3.2.

3.1 Effects of the warp function smoothness

The analytical formulation described in the previous section allows to estimate the actual offset in pixels along slant range, $\Delta p = p_S - p_M$, between master and slave images, at any slow time instant. Therefore, the effectiveness of any kind of warp function in terms of its capability to fit the true geometric distortions may be analyzed w.r.t. any terrain profile. In particular, our investigation is restricted to warp functions $\Delta\tilde{p}_{\rm pol}$ described by polynomials of a certain degree n, whose coefficients A_k are estimated in order to best fit (least-mean-squares approach) the actual offset trend Δp, from near to far range:

$$\Delta p \approx \Delta\tilde{p}_{\rm pol} = \sum_{k=0}^{n} A_k p_M^k. \tag{15}$$

Since range offsets Δp are directly proportional to the range sampling rate f_s (eq. (7)), and the polynomial coefficients A_k are estimated through a LMS procedure, it is possible to proof that also the polynomial coefficients A_k are directly proportional to f_s. Therefore:

$$\Delta\tilde{p}_{\mathrm{pol}} = f_s \sum_{k=0}^{n} a_k p_M^k. \tag{16}$$

where coefficients a_k are, therefore, not anymore dependent on the range sampling rate considered. The smoothness of the polynomial warp function is obviously inadequate for modeling geometric distortions in case of rough topography and long baselines, leading to local misregistrations, $(\Delta p - \Delta\tilde{p}_{\mathrm{pol}})$, as much as higher is f_s.

Actually, the fit is also poor for very regular terrain profiles, in case of high normal baselines and strong differences between the maximum and the minimum topographic height over the scene, ΔH_G. This can be shown by modeling the terrain profile over the entire swath as a raised cosine, centered at mid-range and with spatial period equal to the swath width. Results are summarized in Figs. 3a-b for SAR sensors with different carrier frequencies, as well as spatial resolution, range sampling rate and swath covered, a topographic range ΔH_G of 1 km, over the entire swath, and polynomial degrees $n \in \{2, 3\}$.

By fixing the baseline B (1 km in Fig. 3) and varying the baseline orientation angle α from 0 to 360 degrees, maximum misregistrations may be derived for the entire range of normal baselines $|B_\perp|$ from 0 to B. So, for any baseline orientation angle, normal baseline and offset residual values can be derived from the polar diagrams in Fig. 3a and -b. The plots show that offset residuals increase with the normal baseline $|B_\perp|$, the height range ΔH_G over the scene, and the range sampling rate, as expected. Actually, a fair comparison among the three bands can be done only by assuming an identical value for the incidence angle. Because of the multi-beam capability of new L- or X-band SAR sensors, all simulations refer to the particular beams of the real data processed (see Sec. 4.1). This explains why, despite the doubled chirp bandwidth, the entity of misregistrations for a given parameter triplet for ALOS $\{|B_\perp|, \Delta H_G, n\}$ is comparable (see Fig. 3b) to the corresponding residuals for the ERS satellite. ALOS simulations refer, indeed, to an incidence angle of ~ 38.7 degrees, while the same angle is only ~ 23.2 deg for ERS data.

A DEM-assisted approach seems to be absolutely necessary for a proper coregistration of X-band SAR images, even in case of moderate values for $|B_\perp|$ and ΔH_G, since offset residuals cannot be reduced under 1/8 pixel with a polynomial of reasonable degree (i.e., no more than 3). In spite of a slant range resolution five times lower than TerraSAR-X, even the coregistration of ALOS interferograms is expected to be significantly improved since, actually, SLC pairs with normal baselines of few kilometers are not unusual for this sensor (the ALOS critical baseline is $\sim$ 15km – Tab. 1). Misregistrations more than 1/8 pixel never occur, instead, for ERS images, with a third degree polynomial and a topographic range of 1km, even with normal baselines near to the critical baseline ($\sim$ 1.1 km, for ERS). Nevertheless, even for ERS images, the minimum required accuracy for a proper coregistration is hardly achievable with higher topographic ranges and/or a second degree polynomial.

3.2 DEM error analysis

The height information in the radarcoded DEM is affected by errors mainly due to the intrinsic finite vertical accuracy of the Digital Elevation Model, and, to a lesser degree, to the accuracy of the radarcoding procedure. For instance, the Shuttle Radar Topography Mission (SRTM) provided DTED-2 DEMs, with a posting of 90×90 meters (outside USA) and 15 m absolute height resolution for most of the Earth's surface; as we will see, such accuracy is sufficient for our registration purposes. In this section we estimate the entity of offset residuals for a given height error. First of all, let us indicate with p_S the slave pixel number corresponding to a generic master pixel number p_M, estimated theoretically under the analytical formulation introduced above, and assuming to know exactly the height of each pixel. The relative offset, $\Delta p = p_S - p_M$, can be determined through eq. (5), once the slant range distance between the slave satellite position and the ground point G, $R_{S,G}$, has been estimated. Since DEM errors δH_G (setting $\tilde{H}_G = H_G + \delta H_G$) affect the slave slant range estimation, $\tilde{R}_{S,G}$, erroneous values are estimated for the slave pixel number, $\tilde{p}_S$, w.r.t. the same master pixel number p_M, and so for the estimated offset, $\Delta\tilde{p}_{\mathrm{dem}} = \tilde{p}_S - p_M$, leading to misregistrations:

$$p_S = 2\frac{f_s}{c} R_{S,G} - f_s\,\tau_{S0}, \qquad \tilde{p}_S = 2\frac{f_s}{c} \tilde{R}_{S,G} - f_s\,\tau_{S0}$$

The entity of the misregistration, $(\Delta\tilde{p}_{\mathrm{dem}} - \Delta p)$, is therefore equal to:

$$(\Delta\tilde{p}_{\mathrm{dem}} - \Delta p) = \tilde{p}_S - p_S = 2\frac{f_s}{c}(\tilde{R}_{S,G} - R_{S,G})\,. \tag{17}$$

Assuming moderate height errors, a linear approximation becomes acceptable:

$$\tilde{R}_{S,G} \simeq R_{S,G} + \frac{\partial R_{S,G}}{\partial H_G}\,\delta H_G\,, \qquad (\Delta\tilde{p}_{\mathrm{dem}} - \Delta p) = 2\frac{f_s}{c}\frac{\partial R_{S,G}}{\partial H_G}\,\delta H_G\,, \tag{18}$$

According to the geometrical model described in Sec. 2.1, the following equation for the slave slant range variation w.r.t. the topographic height can be derived:

$$\frac{\partial R_{S,G}}{\partial H_G} = \frac{1}{R_{S,G}}\left[(H_G + \rho) - (H_S + \rho)\,\xi\right], \tag{19}$$

where

$$\xi = \cos\left(\delta_{M,G} - \delta_{M,S}\right)\left(1 - \tan\delta_{M,G}\tan(\delta_{M,G} - \delta_{M,S})\,\zeta(H_G, H_M, \rho, R_{M,G})\right), \tag{20}$$

with

$$\zeta(H_G, H_M, \rho, R_{M,G}) = \frac{\left[(H_G+\rho)^2 - \left((H_M+\rho)^2 - R_{M,G}^2\right)\right]\left[(H_G+\rho)^2 + \left((H_M+\rho)^2 - R_{M,G}^2\right)\right]}{\left[(H_G+\rho)^2 - \left((H_M+\rho) + R_{M,G}\right)^2\right]\left[(H_G+\rho)^2 - \left((H_M+\rho) - R_{M,G}\right)^2\right]}. \tag{21}$$

This formulation is extendable to the more accurate geometrical model described in Sec. 2.2, by applying the substitutions in eq. (14). As for the offset residuals due to the warp function smoothness, also the residuals due to the DEM errors are directly proportional to the range sampling rate (eq. (18)). Moreover, by varying the baseline orientation angle α from 0 to 360 degrees, the influence of DEM errors on the coregistration accuracy may be derived for a range of normal baselines. Fig. 3c illustrates the misregistration trends due to DEM errors in C, L and X band, w.r.t. the NASA SRTM DEM vertical accuracy and by varying the topographic height range ΔH_G equal to 1 km. It can be proof that the influence of H_G in eqs. (17)–(20) is very weak. Therefore, a simplified but well-approximated expression for the factor $\zeta(H_G, H_M, \rho, R_{M,G})$ can be retrieved by imposing $H_G = 0$.

As shown in Figs. 3b–c, the entity of misregistrations $(\Delta\tilde{p}_{\mathrm{pol}} - \Delta p)$, in case of a polynomial warp function of second or third degree, are, in all three bands, well above the offset residuals $(\Delta\tilde{p}_{\mathrm{dem}} - \Delta p)$ due to DEM errors, by assumption not exceeding ~ 15 m, i.e. the nominal SRTM vertical accuracy. This is much more evident in Fig. 3d, where the ratio $(\Delta\tilde{p}_{\mathrm{pol}} - \Delta p)/(\Delta\tilde{p}_{\mathrm{dem}} - \Delta p)$ is plotted for the three bands. This ratio does not depend on the range sampling rate, because of the linear dependency on f_s of both offset residuals at numerator and denominator. Therefore, differences among ERS, ALOS, and TerraSAR plots in Fig. 3d are mainly due to the different look angles, satellite heights and covered swaths among the sensors. As shown in Fig. 3d, even with a third degree polynomial, misregistrations due to DEM errors are more than ten times less than the offset residuals due to the polynomial smoothness. In case of rough topography, we suggest, therefore, a DEM-assisted approach as the preferred method for coregistration of high resolution images (X-band), as well as for coarser resolution images (L- and C-band). The vertical accuracy of NASA SRTM DEMs can therefore be considered acceptable for a successful DEM-assisted coregistration, still in case of high-resolution SAR images. Actually, the referred vertical accuracy of NASA SRTM DEMs should be considered as an optimistic estimate, since it refers to a ground resolution much coarser than that of the SAR sensor, even for ERS images (i.e., the SAR images with the worst resolution, compared to the other L- or X-band SAR sensors investigated). DEM errors may be therefore much higher in practice, still discarding those introduced by an erroneous DEM radarcoding, by themselves not quite negligible. This means that, especially for ERS images (where misregistrations due to smooth warp functions are the weakest among the SAR sensors considered in the present work, because of the lower range sampling rate), the improvements introduced by the DEM-assisted coregistration may be less significant in practice.

4. REAL DATA PROCESSING

We recall that the complex coherence γ is defined as:[1]

$$\gamma = \frac{E[s_1 s_2^*]}{\sqrt{E[s_1 s_1^*]}\sqrt{E[s_2 s_2^*]}} \tag{22}$$

where s_1 and s_2 are the two complex SAR signals. Assuming ergodicity, it can be estimated through the following:

$$\gamma \approx \frac{\langle s_1 s_2^* \exp[-j\phi] \rangle}{\sqrt{\langle s_1 s_1^* \rangle \langle s_2 s_2^* \rangle}} \tag{23}$$

where the average operation is performed spatially, and ϕ is a phase component including effects of topography, displacement, and any residual phase not constant within the estimation window. It can be shown[8] that γ can be factorized in terms of the sources of decorrelation as follows:

$$\gamma = \gamma_{\text{temporal}} \cdot \gamma_{\text{geom}} \cdot \gamma_{DC} \cdot \gamma_{\text{vol}} \cdot \gamma_{\text{thermal}} \cdot \gamma_{\text{processing}} \tag{24}$$

(see Ref. 1 for a detailed description of each decorrelation contribution). Misregistrations, as well as errors occurring during interpolation, translate in a loss of coherence, expressed by the decorrelation contribution $\gamma_{\text{processing}}$. Therefore coherence estimation may be used in order to compare the DEM-assisted coregistration potentials w.r.t. the standard approach, where a 2-D polynomial of a certain degree (we use second degree in the results shown further on) is used in order to model the warp function between master and slave. However, this contribution will be hardly discernible in case the other sources of decorrelation play an important role. Indeed, let us indicate with $\tilde{\gamma}$ (resp., $\hat{\gamma}$) the coherence map evaluated for the interferograms obtained by coregistering the images in the standard way (resp., through the DEM-assisted procedure). The difference between the coherence maps estimated with the two methodologies is therefore given by:

$$\begin{aligned} \tilde{\gamma} - \hat{\gamma} &= \gamma_{\text{temporal}} \cdot \gamma_{\text{geom}} \cdot \gamma_{Dc} \cdot \gamma_{\text{vol}} \cdot \gamma_{\text{thermal}} \cdot (\tilde{\gamma}_{\text{processing}} - \hat{\gamma}_{\text{processing}}) \\ &= \Gamma \cdot (\tilde{\gamma}_{\text{processing}} - \hat{\gamma}_{\text{processing}}) \end{aligned} \tag{25}$$

Our goal is to measure the quantity $(\tilde{\gamma}_{\text{processing}} - \hat{\gamma}_{\text{processing}})$, but this is actually weighted by Γ. Therefore, a comparison between DEM-assisted and standard coregistration approaches will be more feasible as Γ is close to 1.

4.1 Data sets description

For a complete assessment of the potentials of the DEM assisted coregistration, our investigation has been extended over C, L, and X-band interferograms, using sensors with very different spatial resolutions (see tab. 1 for details).

To minimize the temporal decorrelation, only interferometric pairs with a temporal baseline equal to the corresponding orbital repeat cycle have been chosen. For the COSMO/SkyMed pair and the Umbria Test Site, moreover, the temporal baseline has been even halved w.r.t. the repeat cycle of a single satellite, since the master and slave SAR images have been acquired by the two satellites of the constellation so far in orbit, flying in interferometric configuration. All the interferograms generated in C and X band cover a quarter of the full frame. In L band, instead, the entire full frame has been considered. A coherence estimator window of 11×11 pixels has been used.

All tests have been performed through use of the DEM-assisted technique developed at TU-Delft[3] and included in the DORIS open source SAR interferometric processing tool.[5] For all the test sites, DTED-2 DEMs provided by the Shuttle Radar Topography Mapping (SRTM) mission, with 3" posting in latitude and longitude, have been used for estimating the warp function with the DEM-assisted coregistration approach. In Fig. 4, coherence maps obtained by standard and geometric coregistration approaches are compared. In Fig. 5, further comparisons are made through scatter plots and histograms.

4.2 Results

As expected from the simulations described in Sec. 3, in X band, smooth warp functions such as 2-D polynomials of low degree cannot ensure a sub-pixel coregistration accuracy. The peak of the Ol Doinyo Lengai volcano in Tanzania, for example, is clearly visible in the DEM-Assisted coherence map, but absolutely dark (i.e., very low coherence) in the case of the TerraSAR-X InSAR pair coregistered in the standard way. It is interesting to note that improvements in coregistration involve also the Kerimasi volcano, more to the north (Fig. 4), as can be noticed by the increased coherence on its slopes, indicated by the white arrow. Nevertheless, around the Kerimasi crater, the differences between the two methodologies are not substantial. The volcano is very vegetated, so temporal and volumetric decorrelation heavily affect our capability to discriminate the difference $(\tilde{\gamma}_{\text{processing}} - \hat{\gamma}_{\text{processing}})$, as suggested by eq. (25). In case of the COSMO/SkyMed interferogram (Test Site: Umbria), the widespread improvements obtained with the DEM-assisted coregistration may be explained in terms of the normal baseline, the highest among the X-band interferograms, even though the topographic range over the entire scene is less than half of the corresponding value for the TerraSAR-X test site (see tab. 1). We have also to take into account the reliability of the offsets initially estimated for a number of patches over the master and slave images in the standard coregistration approach, as we will discuss briefly in the last section. Obviously, standard coregistration in X band is still acceptable in case of limited normal baselines and gentle slopes, as is the case for the other COSMO/SkyMed test site (Rome, Fig. 4).

ERS coherence maps, on the other hand, do not show any significant improvement, as already assessed in Ref. 3. This does not mean that improvements are totally absent. Again, a reliable DEM-assisted coregistration assessment can be done, provided the other decorrelation factors are negligible. Coregistration improvements due to a DEM-assisted approach are significant at high normal baselines, where the geometric decorrelation is predominant, because of the very low critical baseline (only ~ 1.1 km for ERS). On the other hand, by processing interferograms with low normal baselines, we reduce the geometric decorrelation but, in this case, also a smooth polynomial is acceptable as warp function.

In spite of the lower carrier frequency of ALOS PALSAR w.r.t. ERS, the doubled chirp bandwidth ensures higher range resolution and posting. Furthermore, thanks to a critical baseline of ~ 15 km, geometric decorrelation is still very low with normal baselines of a few kilometers. Also the temporal decorrelation,[9] as well as the volumetric one are much more reduced than in C and X bands, because of the higher wavelength. Therefore, even with a 3-times coarser ground range resolution than in X band (tab. 1), quite significant improvements in the interferometric coherence may be appreciated (see Fig. 4).

5. CONCLUSIONS

An assessment of the performances of a geometrical DEM-assisted coregistration with respect to more traditional approaches (warp functions modeled as 2-D polynomials) has been carried out in this study. In particular, the impact of range sampling rate, topographic range over the covered swath, and DEM errors, on the final coregistration precision has been evaluated for different radar postings and relative positions of satellites, through both analytical relationships and simulations. The two coregistration approaches have been compared by processing real data in C, L and X band, using the interferometric coherence as quality figure. In X band, considerable improvements have been found by coregistering the images through the DEM-assisted approach, even with DTED-2 Digital Elevation Models, as those provided by the NASA SRTM mission. Improvements are noticed also in L band (ALOS), while in C band (ERS) are not so evident. As processing decorrelation has to be minimized even in case the other sources of decorrelation are negligible, DEM-assisted coregistration is, therefore, recommended, especially in case of long normal baselines and rough topography. In particular, for X band interferometry, this approach is absolutely to be preferred than the standard one. Furthermore, the DEM-assisted technique, developed at TU Delft and included in DORIS, is also capable to estimate and correct for the timing errors between master and slave.[3] Finally, it is important to notice that, in the standard approach, the smoothness of the polynomial warp function is not the only cause of misregistration, since the quality of coregistration depends, in this case, also on the amount and distribution of the windows to find the offsets. Indeed, a poor global quality of the coregistration model may be also due to a wrong preliminary tie-point matching between master and slave. This is e.g. the case of the COSMO/SkyMed interferogram in Umbria, where the focused images are not radiometrically equalized (SCS_U imagery).

ACKNOWLEDGMENTS

TerraSAR data (©Infoterra) were kindly provided by Infoterra and acquired (Sales Order Number 5832) in the framework of the SAMAAV project (Study And Monitoring of Active African Volcanoes) coordinated by Royal Museum for Central Africa in Belgium and National Museum of Natural History of Luxembourg (contacts: francois.kervyn@africamuseum.be and nicolas.doreye@ecgs.lu). PALSAR images provided by European Space Agency (ESA) under the ALOS ADEN AO 3595 project. ERS data provided by ESA under the CAT-1 project n.2653. The authors thank Antonio Valentino of the Consortium Innova (Italy) for the fruitful collaboration.

REFERENCES

[1] Hanssen, R. F., [*Radar Interferometry: Data Interpretation and Error Analysis*], Kluwer Academic Publishers, Dordrecht (2001).

[2] Leberl, F. W., [*Radargrammetric Image Processing*], Artech House Inc., Norwood MA, 1st ed. (1990).

[3] Arikan, M., van Leijen, F., Guang, L., and Hanssen, R. F., "Improved image alignment under the influence of elevation," *Proceedings of FRINGE 2007* (2007).

[4] Eineder, M., Adam, N., and Yague-Martinez, N., "First TerraSAR-X interferometry evaluation," *Proceedings of FRINGE 2007* (2007).

[5] Kampes, B. M., Hanssen, R. F., and Perski, Z., "Radar interferometry with public domain tools," *Proceedings of FRINGE 2003* (2003).

[6] Euler, L., "Recherches sur la courbure des surfaces," *Mémoires de l'academie des sciences de Berlin* **16**, 119–143 (1767).

[7] Meusnier, J., "Mémoire sur la courbure des surfaces," *Mémoires des savans étrangers* **10**, 477–510 (1785).

[8] Zebker, H. A. and Villasenor, J., "Decorrelation in interferometric radar echoes," *IEEE Transactions on Geoscience and Remote Sensing* **30**, 950–959 (Sept. 1992).

[9] Ferretti, A., Colesanti, C., Perissin, D., Prati, C., and Rocca, F., "Evaluating the effect of the observation time on the distribution of SAR permanent scatterers," *Proceedings of FRINGE 2003* (2003).

Table 1. *Processed stripmap SLC datasets.* Test Sites: [1] Mt.Vesuvio, Italy (ERS-2); [2] Daunia, Italy (ALOS); [3] Ol Doinyo Lengai, Tanzania (TerraSAR-X, ©Infoterra); [4] Umbria, Italy (CSK-S1&2 - pol.VV); [5] Rome, Italy (CSK-S1 - pol.HH). Notation: $B_t \equiv$ temporal baseline, $B_\perp \equiv$ normal baseline, $B_{\perp,c} \equiv$ critical baseline, $\Phi \equiv$ master scene center longitude, $\Lambda \equiv$ master scene center latitude, $H_M \equiv$ master satellite height , $\Delta H_G \equiv$ topographic range over the entire processed scene, $\theta_{inc} \equiv$ incidence angle, $R_{gr} \equiv$ ground range resolution, $R_{az} \equiv$ azimuth resolution, $A/D \equiv$ Asc./Desc.

#	Sensor	MASTER Date [dd.mm.yy]/Orbit	SLAVE Date [dd.mm.yy]/Orbit	A/D	B_t	$\lvert B_\perp \rvert$	Φ	Λ	H_M	ΔH_G
1	ERS-2	25.11.95/3125	30.12.95/3626	D	35	$\sim$ 860 m	40.951°N	14.756°E	$\sim$ 789 km	$\sim$ 1600 m
2	PSR	10.01.07/5132	25.02.07/5803	A	46	$\sim$ 1860 m	41.589°N	14.839°E	$\sim$ 700 km	$\sim$ 1600 m
3	TSX	05.05.08/4942	16.05.08/5109	A	11	$\sim$ 315 m	2.779°S	3.594°E	$\sim$ 512 km	$\sim$ 2130 m
4	CSK	04.04.08/1735 [S2]	12.04.08/4579 [S1]	A	8	$\sim$ 800 m	42.945°N	12.051°E	$\sim$ 628 km	$\sim$ 900 m
5	CSK	22.09.07/1572 [S1]	08.10.07/1809 [S1]	A	16	$\sim$ 430 m	41.932°N	12.461°E	$\sim$ 628 km	$\sim$ 150 m

#	Sensor	Frequency Band	Pol.	Chirp BW	θ_{inc} (beam ID)	$B_{\perp,c}$	R_{gr}	R_{az}	Swath
1	ERS-2	C (5.3 GHz)	VV	15.55 MHz	$\sim 23.2°$	$\sim$ 1.10 km	$\sim$ 24.5 m	$\sim$ 5.0 m	$\sim$ 100 km
2	PSR	L (1.27 GHz)	HH	28 MHz	$\sim 38.7°$ (#8)	$\sim$ 15.38 km	$\sim$ 8.6 m	$\sim$ 5.0 m	$\sim$ 70 km
3	TSX	X (9.65 GHz)	HH	150 MHz	$\sim 26.3°$ (#5)	$\sim$ 4.33 km	$\leq$ 3.0 m	$\leq$ 3.0 m	$\sim$ 30 km
4	CSK	X (9.60 GHz)	VV	85 MHz	$\sim 41.4°$ (H4-10)	$\sim$ 6.32 km	$\leq$ 3.0 m	$\leq$ 3.0 m	$\sim$ 40 km
5	CSK	X (9.60 GHz)	HH	102 MHz	$\sim 34.0°$ (H4-05)	$\sim$ 5.33 km	$\leq$ 3.0 m	$\leq$ 3.0 m	$\sim$ 40 km

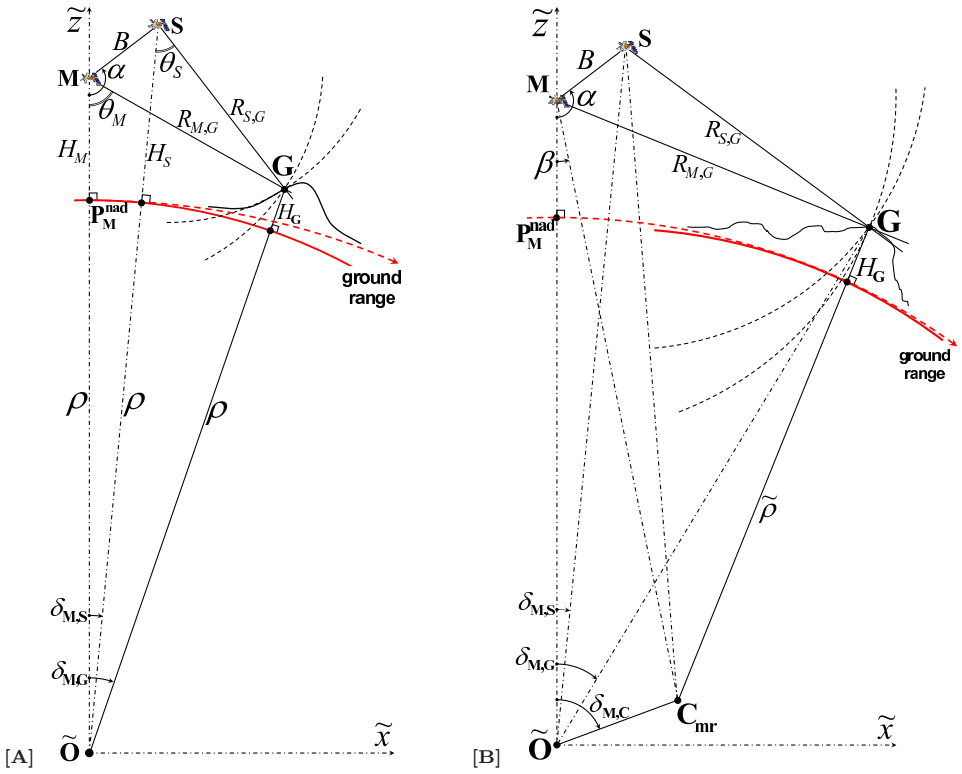

Figure 1. SAR interferometric geometry. (A) The elliptic cross section (dashed red line) between the reference ellipsoid (WGS84) and the zero-Doppler plane π is approximated with a circle (solid red line) centered in $\tilde{O}$, the curvature center of the ellipse w.r.t. the nadir projection $P_M^{\rm nad}$ of the master satellite position. The position of the slave satellite is provided in terms of the distance B (or baseline) and the baseline orientation angle α, measured from the master nadir-direction towards the its looking direction. In (B), instead, the elliptic cross section is approximated with a circle (solid red line) centered in $C_{\rm mr}$, i.e. the curvature center of the ellipse w.r.t. the nadir projection of the point G_{mr}, located at mid-range.

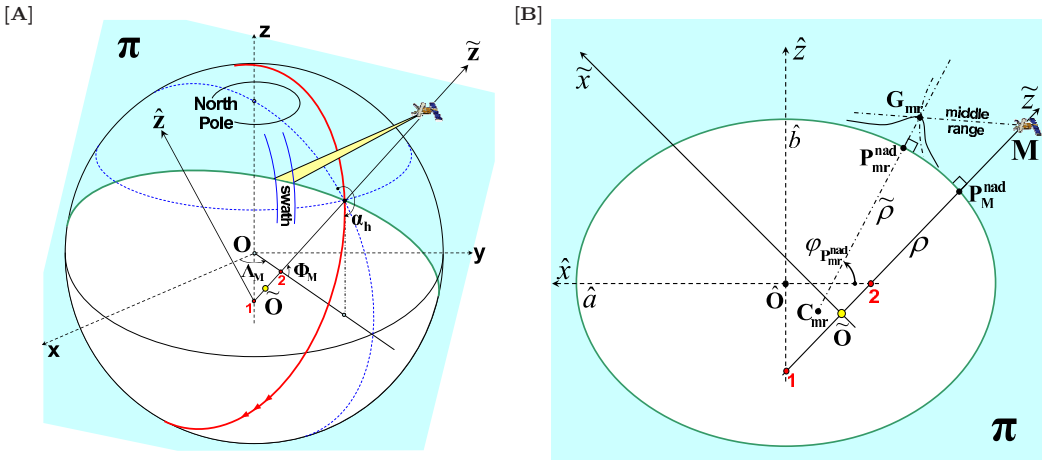

Figure 2. (A) 3D view of the SAR acquisition mode (stripmap mode). For a given azimuth time, the scene imaged by the radar along the line of sight (LOS) belongs to the zero-Doppler plane π (in pale-blue). Because of the side-looking acquisition mode of SAR sensors and the assumption of zero-Doppler (deskewed) stripmap imaging geometry, the azimuth angle of the cross section π is equal to $(\alpha_h + \pi/2)$ (in case of right looking), with α_h heading of the orbit. (B) 2D view of the cross section π. $\tilde{O}$ and $C_{\rm mr}$ are the curvature centers in the nadir projections, $P_M^{\rm nad}$ and $P_{\rm mr}^{\rm nad}$, of the master satellite position and the ground point at middle range, respectively. In practice, $\tilde{O}$ will be always located between points **1** (i.e., center of curvature of the prime vertical in $P_M^{\rm nad}$) and **2**, depending on the particular azimuth angle of the section π.

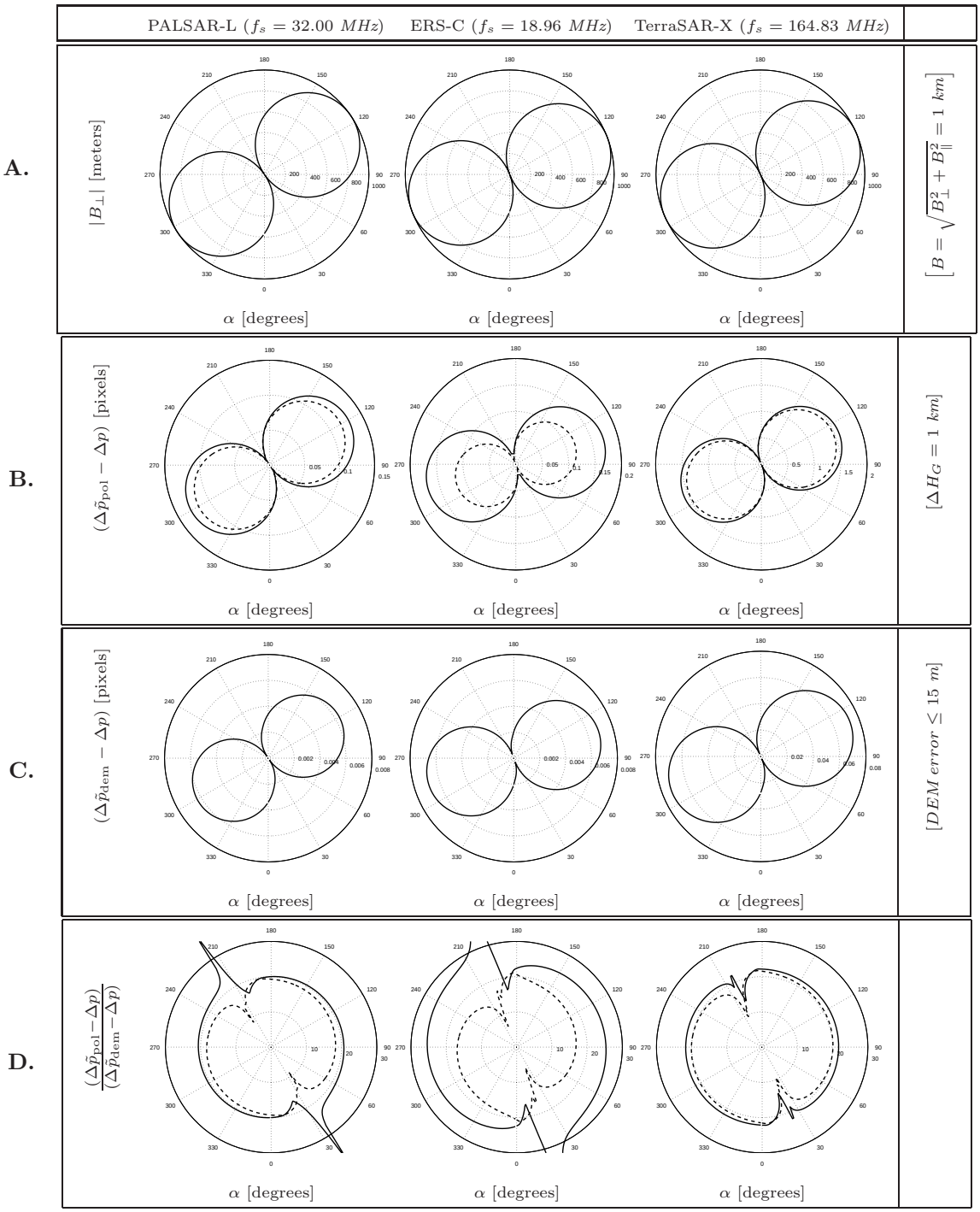

Figure 3. [A] Polar Diagrams of the absolute normal baselines $|B_\perp|$ at mid-range for different master-slave configurations, obtained by varying the baseline orientation angle α from 0 to 360 degrees (constant distance $B = 1$km between master and slave). [B] Polar diagrams of the offset residuals estimated for polynomial warp functions with degrees 2 (solid line) and 3 (dashed line), corresponding to each pair $(\{\alpha, |B_\perp|\})$ in [A] (the topographic range ΔH_G is assumed to be equal to 1 km). [C] Plots of the offset residuals due to inaccurate knowledge of the topographic profile, by assuming the vertical accuracy of SRTM DEMs. All simulated offsets in [B] and [C] have been derived w.r.t. look angles of the real data processed in Sec. 4 (table 1). [D] Ratio between the offset residuals due to the smoothness of the polynomial function and the corresponding residuals due to DEM errors. Since for each pair $(\{\alpha, |B_\perp|\})$ this ratio is much higher than 1, performances of the DEM-A coregistration are always better than the standard approach.

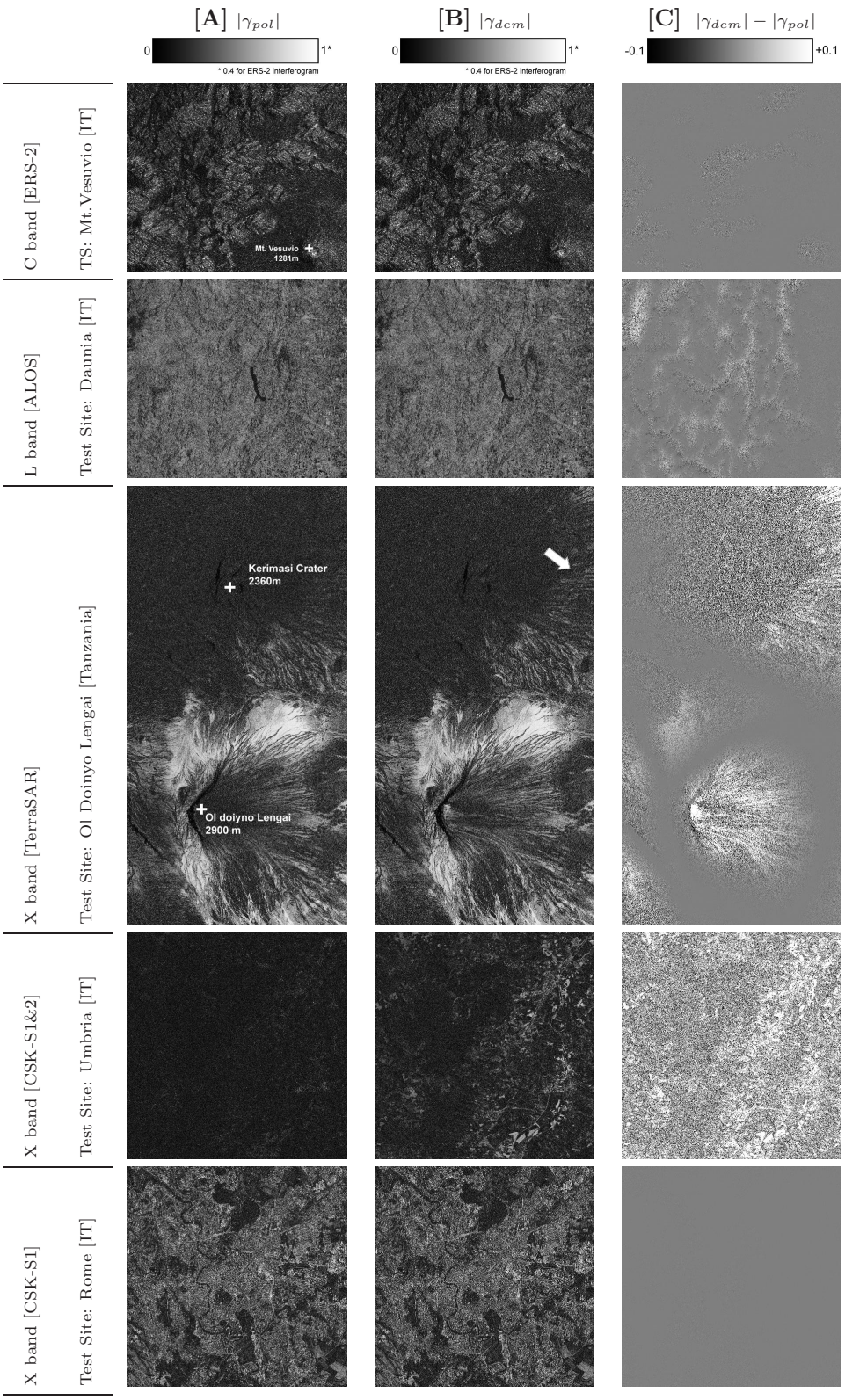

Figure 4. Comparisons between standard (2-D polynomial warp function) and DEM-assisted coregistration (see Tab. 1 for processed data sets parameters). [A] Coherence maps obtained with standard coregistration. [B] Coherence maps obtained with DEM-Assisted coregistration. [C] Coherence improvement of the geometric over the standard approach.

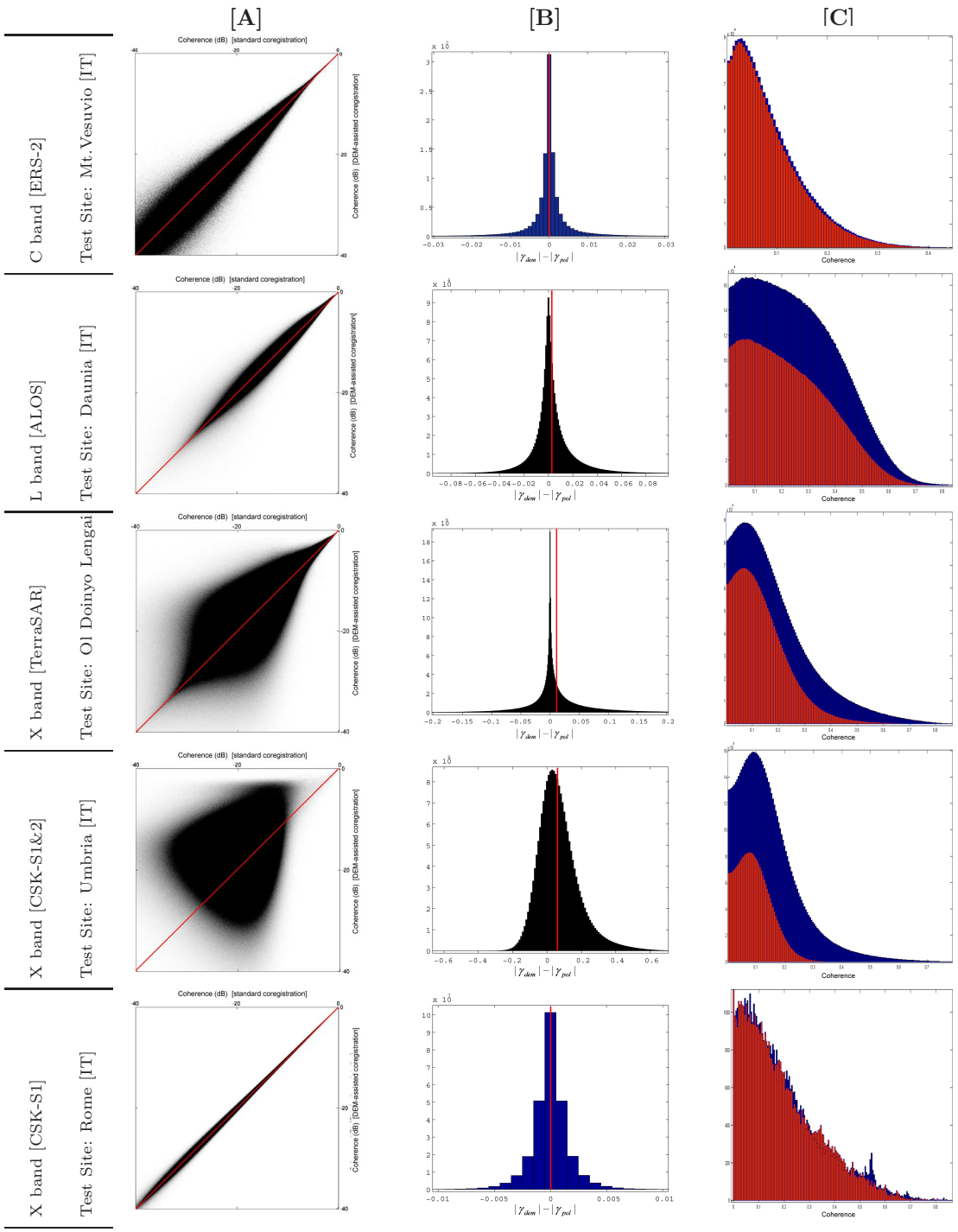

Figure 5. [A] Scatter plots of coherence values obtained using polynomial based coregistration (degree 2) vs. the DEM assisted ones, for all bands and test sites (see Tab. 1). [B] Histograms of the differences $|\gamma_{dem}| - |\gamma_{pol}|$ between coherence values obtained with the two coregistration approaches. The vertical red line shows the mean value of the differences. [C] In blue are plotted the histograms of the coherence values obtained with the DEM-A approach, for all pixels where $|\gamma_{dem}| \geq |\gamma_{pol}| + \gamma_{th}$. The threshold γ_{th} has been chosen equal to 0.01, in order to take into account the coherence estimation noise. In red are plotted, instead, the histograms of the coherence values obtained with the standard approach, for pixels where $|\gamma_{pol}| \geq |\gamma_{dem}| + \gamma_{th}$. Since the numbers of pixels where $|\gamma_{dem}| \geq |\gamma_{pol}| + \gamma_{th}$ and $|\gamma_{pol}| \geq |\gamma_{dem}| + \gamma_{th}$ are not equal, in general, red and blue histograms have different areas. Bigger is the area of the "blue" histogram w.r.t. the red one, better are the performances of the DEM-A coregistration w.r.t. the standard approach.